4604 *Inorg. Chem.* **2001,** *40,* 4604−4616

Mixed-Valence Tetranuclear Manganese Single-Molecule Magnets

Jae Yoo,[1a] Akira Yamaguchi,[1b] Motohiro Nakano,[1a] J. Krzystek,[1c] William E. Streib,[1d]
Louis-Claude Brunel,[1c] Hidehiko Ishimoto,[1b] George Christou,*,[1d] and
David N. Hendrickson*,[1a]

Department of Chemistry and Biochemistry - 0358, University of California at San Diego, La Jolla, California 92093, Institute of Solid State Physics, The University of Tokyo, 7-22-1 Roppongi, Minatoku, Tokyo 106-8666, Japan, Center for Interdisciplinary Magnetic Resonance, National High Magnetic Field Laboratory, Tallahassee, Florida 32310, and Department of Chemistry and Molecular Structure Center, Indiana University, Bloomington, Indiana 47405

Received November 15, 2000

The preparations, X-ray structures, and detailed physical characterizations are presented for two new mixed-valence tetranuclear manganese complexes that function as single-molecule magnets (SMM's): $[Mn_4(hmp)_6Br_2(H_2O)_2]Br_2{\cdot}4H_2O$ **(2)** and $[Mn_4(6\text{-me-hmp})_6Cl_4]{\cdot}4H_2O$ **(3)**, where hmp^- is the anion of 2-hydroxymethylpyridine and 6-me-hmp^- is the anion of 6-methyl-2-hydroxymethylpyridine. Complex **2**$\cdot 4H_2O$ crystallizes in the space group $P2_1/c$, with cell dimensions at −160 °C of $a = 10.907(0)$ Å, $b = 15.788(0)$ Å, $c = 13.941(0)$ Å, $\beta = 101.21(0)°$, and $Z = 2$. The cation lies on an inversion center and consists of a planar Mn_4 rhombus that is mixed-valence, $Mn_2^{III}Mn_2^{II}$. The hmp^- ligands function as bidentate ligands and as the only bridging ligands in **2**$\cdot 4H_2O$. Complex **3**$\cdot 4H_2O$ crystallizes in the monoclinic space group $C2/c$, with cell dimensions at −160 °C of $a = 17.0852(4)$ Å, $b = 20.8781(5)$ Å, $c = 14.835(3)$ Å, $\beta = 90.5485(8)°$, and $Z = 4$. This neutral complex also has a mixed-valence $Mn_2^{III}Mn_2^{II}$ composition and is best described as having four manganese ions arranged in a bent chain. An μ_2-oxygen atom of the 6-me-hmp^- anion bridges between the manganese ions; the Cl^- ligands are terminal. Variable-field magnetization and high-frequency and -field EPR (HFEPR) data indicate that complex **2**$\cdot 4H_2O$ has a $S = 9$ ground state whereas complex **3**$\cdot 4H_2O$ has $S = 0$ ground state. Fine structure patterns are seen in the HFEPR spectra, and in the case of **2**$\cdot 4H_2O$ it was possible to simulate the fine structure assuming $S = 9$ with the parameters $g = 1.999$, axial zero-field splitting of $D/k_B = -0.498$ K, quartic longitudinal zero-field splitting of $B_4^o/k_B = 1.72 \times 10^{-5}$ K, and rhombic zero-field splitting of $E/k_B = 0.124$ K. Complex **2**$\cdot 4H_2O$ exhibits a frequency-dependent out-of-phase AC magnetic susceptibility signal, clearly indicating that this complex functions as a SMM. The AC susceptibility data for complex **2**$\cdot 4H_2O$ were measured in the 0.05−4.0 K range and when fit to the Arrhenius law, gave an activation energy of $\Delta E = 15.8$ K for the reversal of magnetization. This ΔE value is to be compared to the potential-energy barrier height of $U/k_B = |D\hat{S}_Z^2| = 40.3$ K calculated for **2**$\cdot 4H_2O$.

Introduction

Single-molecule magnets (SMM's) are of considerable interest because they could serve as small magnetic memory units.[2,3] SMM's are also being studied since they provide a means to systematically study the chemistry and physics of nanomagnets.[3] SMM's can be viewed as slowly relaxing magnetic particles of well-defined size and shape. The slow magnetization relaxation of a SMM is due to the presence of an energy barrier for the reversal of the direction of its magnetization. The magnetization of a molecule that functions as a SMM can be either aligned "spin-up" or "spin-down" relative to the principal axis of magnetization of the molecule. In simple terms, such a molecule has a large spin (S) ground state and the barrier for flipping the magnetic moment from "spin-up" to "spin-down" is due to a Ising type magnetic anisotropy characterized by $D\hat{S}_Z^2$, where $D < 0$. The potential energy diagram for a $S = 9$ SMM is shown in Figure 1, where the minimum with $M_s = -9$ on the left corresponds to the "spin-up" state and the minimum ($M_s = +9$) on the right of the energy barrier is the "spin-down" state. The height of the energy barrier is given by $|D\hat{S}^2|$. The origin of the magnetic anisotropy ($D\hat{S}_Z^2$) is single-ion zero-field splittings at the Mn atom sites in the molecule. At low temperatures, the conversion from "spin-up" to "spin-down" becomes sluggish and this results in the appearance of an out-of-phase AC magnetic susceptibility signal and magnetization hysteresis loops.

The first molecule shown to be a SMM is $[Mn_{12}O_{12}(O_2CMe)_{16}(H_2O)_4]{\cdot}4H_2O{\cdot}2HO_2CCH_3$,[4] named Mn_{12}Ac in the literature,[5−51] which exhibits slow magnetization relaxation due

---

* To whom correspondence should be addressed.

(1) (a) University of California, (b) Institute of Solid State Physics, The University of Tokyo, (c) National High Magnetic Field Laboratory, (d) Indiana University.

(2) Dahlberg, E. D.; Zhu, J.-G *Phys. Today* **1995**, 34.

(3) Gunther, L. *Phys. World* **1990**, December 28.

(4) Lis, T. *Acta Crystallogr.* **1980**, *B36*, 2042.

(5) Boyd, P. D. W.; Li, Q.; Vincent, J. B.; Folting, K.; Chang, H.-R.; Streib, W. E.; Huffman, J. C.; Christou, G.; Hendrickson, D. N. *J. Am. Chem. Soc.* **1988**, *110*, 8537.

(6) Caneschi, A.; Gatteschi, D.; Sessoli, R.; Barra, A. L.; Brunel, L. C.; Guillot, M. *J. Am. Chem. Soc.* **1991**, *113*, 5873.

(7) Sessoli, R.; Gatteschi, D.; Caneschi, A.; Novak, M. A. *Nature* **1993**, *365*, 141.

(8) Gatteschi, D.; Caneschi, A.; Pardi, L.; Sessoli, R. *Science* **1994**, *265*, 1054.

10.1021/ic0012928 CCC: \$20.00

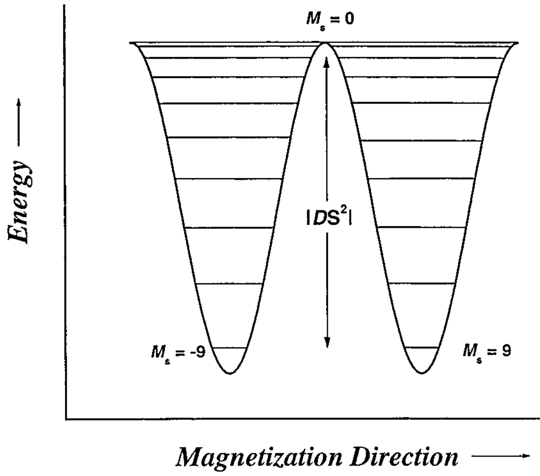

Figure 1. Plot of the potential energy vs magnetization direction for a single-molecule magnet showing the energy barrier separating the "spin-up" and "spin-down" orientations of the magnetic vector along the anisotropy axis.

to a $S = 10$ ground-state split by axial zero-field splitting ($D\hat{S}_Z^2$), where $D/k_B = -0.61$ K. In 1996, Mn_{12}Ac was reported[17−20] to show quantum tunneling of magnetization. Steps at regular intervals of magnetic field are seen in the magnetization hysteresis loops for oriented crystals of Mn_{12}Ac and this generated considerable interest in its magnetic properties.

An important research goal in the field of SMM's has been the discovery of new examples of SMM's. This can lead to the understanding of the factors that govern the magnetization relaxation process. In addition to Mn_{12}Ac, structurally related dodecanuclear manganese SMM's with the composition $[Mn_{12}O_{12}(O_2CR)_{16}(H_2O)_4]$[52−61] and their anionic derivatives, [cation]$[Mn_{12}O_{12}(O_2CR)_{16}(H_2O)_4]$,[62,63] have been characterized. Quantum tunneling of magnetization has been observed for not only the integer spin ground state ($S = 10$) Mn_{12} complexes, but also for the anionic $[Mn_{12}^{-}]$ derivatives with half-integer spin ground states ($S = 19/2$). Several families of tetranuclear SMM's have been discovered as well: a tetranuclear vanadium complex,[64] several manganese complexes with a distorted

---

(9) Villain, J.; Hartman-Boutron, F.; Sessoli, R.; Rettori, A. *Europhys. Lett.* **1994**, *27*, 159.
(10) Barra, A. L.; Caneschi, A.; Gatteschi, D.; Sessoli, R. *J. Am. Chem. Soc.* **1995**, *117*, 8855.
(11) Novak, M. A.; Sessoli, R.; Caneschi, A.; Gatteschi, D. *J. Magn. Magn. Mater.* **1995**, *146*, 211.
(12) Barbara, B.; Wernsdorfer, W.; Sampaio, L. C.; Park, J. G.; Paulsen, C.; Novak, M. A.; Ferre, R.; Mailly, D.; Sessoli, R.; Caneschi, A.; Hasselbach, K.; Benoit, A.; Thomas, L. *J. Magn. Magn. Mater.* **1995**, *140−144*, 1825.
(13) Novak, M. A.; Sessoli, R. In *Quantum Tunneling of Magnetization-QTM'94*; Gunter, L., Barbara, B., Eds.; Kluwer Academic Publishers: Dordrecht, 1995; pp 171−188.
(14) Paulsen, C.; Park, J. G. In *Quantum Tunneling of Magnetization-QTM'94*; Gunther, L., Barbara, B., Eds.; Kluwer Academic Publishers: Dordrecht, 1995; pp 189−207.
(15) Paulsen, C.; Park, J. G.; Barbara, B.; Sessoli, R.; Caneschi, A. *J. Magn. Magn. Mater.* **1995**, *140−144*, 1891.
(16) Politi, R.; Rettori, A.; Hartmann-Boutron, F.; Villain, J. *Phys. Rev. Lett.* **1995**, *75*, 537.
(17) Friedman, J. R.; Sarachik, M. P.; Tejada, J.; Maciejewski, J.; Ziolo, R. *J. Appl. Phys.* **1996**, *79*, 6031.
(18) (a) Friedman, J. R.; Sarachik, M. P.; Tejada, J.; Ziolo, R. *Phys. Rev. Lett.* **1996**, *76*, 3830. (b) Friedman, J. R. Ph.D. Thesis, The City College of New York, New York City, NY, 1996.
(19) Thomas, L.; Lionti, F.; Ballou, R.; Gatteschi, D.; Sessoli, R.; Barbara, B. *Nature* **1996**, *383*, 145.
(20) Tejada, J.; Ziolo, R. F.; Zhang, X. X. *Chem. Mater.* **1996**, *8*, 1784.
(21) Hernandez, J. M.; Zhang, X. X.; Luis, F.; Bartolome, J.; Tejada, J.; Ziolo, R. *Europhys. Lett.* **1996**, *35*, 301.
(22) Chudnovsky, E. M. *Science* **1996**, *274*, 938.
(23) Reynolds, P. A.; Gilber, E. P.; Figgis, B. N. *Inorg. Chem.* **1996**, *35*, 545.
(24) Gatteschi, D. *Curr. Opin. Solid State Mater. Sci.* **1996**, *1*, 192.
(25) Burin, A. L.; Prokof'ev, N. V.; Stamp, P. C. E. *Phys. Rev. Lett.* **1996**, *76*, 3040.
(26) Politi, R.; Rettori, A.; Hartmann-Boutron, F.; Villain, J. *Phys. Rev. Lett.* **1996**, *76*, 3041.
(27) Schwarzschild, B. *Phys. Today* **1997**, January 17.
(28) Lionti, F.; Thomas, L.; Ballou, R.; Barbara, B.; Sulpice, A.; Sessoli, R.; Gatteschi, D. *J. Appl. Phys.* **1997**, *81*, 4608.
(29) Friedman, J. R.; Sarachik, M. P.; Hernandez, J. M.; Zhang, X. X.; Tejada, J.; Molins, E.; Ziolo, R. *J. Appl. Phys.* **1997**, *81*, 3978.
(30) Barra, A. L.; Gatteschi, D.; Sessoli, R. *Phys. Rev. B* **1997**, *56*, 8192.
(31) Luis, F.; Bartolome, J.; Fernandez, J. F. *Phys. Rev. B* **1997**, *55*, 11448.
(32) Hernandez, J. M.; Zhang, X. X.; Luis, F.; Tejada, J.; Friedman, J. R.; Sarachik, M. P.; Ziolo, R. *Phys. Rev. B* **1997**, *55*, 5858.
(33) Cheesman, M. R.; Oganesyan, V. S.; Sessoli, R.; Gatteschi, D.; Thompson, A. *Chem. Commun.* **1997**, 1677.
(34) Caneschi, A.; Gatteschi, D.; Sessoli, R. *J. Chem. Soc., Dalton Trans.* **1997**, 3963.
(35) Zhang, X. X.; Tejada, J.; Hernandez, J. M.; Ziolo, R. F. *Nanostruct. Mater.* **1997**, *9*, 301.
(36) Chudnovsky, E. M.; Garanin, D. A. *Phys. Rev. Lett.* **1997**, *79*. 4469.
(37) Garanin, D. A.; Chudnovsky, E. M. *Phys. Rev. B* **1997**, *56*, 11102.
(38) Wei, Y.-G.; Zhang, S.-W.; Shao, M.-C.; Tang, Y.-Q. *Polyhedron* **1997**, *16*, 1471.
(39) Fominaya, F.; Villain, J.; Gandit, P.; Chaussy, J.; Caneschi, A. *Phys. Rev. Lett.* **1997**, *79*, 1126.
(40) Fort, A.; Rettori, A.; Villain, J.; Gatteschi, D.; Sessoli, R. *Phys. Rev. Lett.* **1998**, *80*, 612.
(41) Lascialfari, A.; Gatteschi, D.; Borsa, F.; Shastri, A.; Jang, Z. H.; Carretta, P. *Phys. Rev. B* **1998**, *57*, 514.
(42) Hill, S.; Perenboom, J. A. A. J.; Dalal, N. S.; Hathaway, T.; Stalcup, T.; Brooks, J. S. *Phys. Rev. Lett.* **1998**, *80*, 2453.
(43) Luis, F.; Bartolome, J.; Fernandez, J. F. *Phys. Rev. B* **1998**, *57*, 505.
(44) Lascialfari, A.; Jang, Z. H.; Borsa, F.; Carretta, P.; Gatteschi, D. *Phys. Rev. Lett.* **1998**, *81*, 3773.
(45) Pederson, M. R.; Khanna, S. N. *Phys. Rev. B* **1999**, *59*, 693.
(46) Zhong, Y.; Sarachik, M. P.; Friedman, J. R.; Robinson, R. A.; Kelley, T. M.; Nakotte, H.; Christianson, A. C.; Trouw, F.; Aubin, S. M. J.; Hendrickson, D. N. *J. App. Phys.* **1999**, *85*, 5636.
(47) Leuenberger, M. N.; Loss, D. *Europhys. Lett.* **1999**, *46*, 692.
(48) Mirebeau, I.; Hennion, M.; Casalta, H.; Andres, H.; Gudel, H. U.; Irodova, A. V.; Caneschi, A. *Phys. Rev. Lett.* **1999**, *83*, 628.
(49) Wernsdorfer, W.; Sessoli, R.; Gatteschi, D. *Europhys. Lett.* **1999**, *47*, 254.
(50) Kent, A. D.; Zhong, Y.; Bokacheva, L.; Ruiz, D.; Hendrickson, D. N.; Sarachik, M. P. *J. App. Phys.* **2000**, *87*, 5493.
(51) Goto, T.; Kubo, T.; Koshiba, T.; Jujii, Y.; Oyamada, A.; Arai, J.; Takeda, K.; Awaga, K. *Physica B* **2000**, 1227.
(52) Eppley, H. J.; Wang, S.; Tsai, H.-L.; Aubin, S. M. J.; Folting, K.; Streib, W. E.; Hendrickson, D. N.; Christou, G. *Mol. Cryst. Liq. Cryst.* **1995**, *274*, 159.
(53) Tsai, H.-L.; Eppley, H. J.; de Vries, N.; Folting, K.; Christou, G.; Hendrickson, D. N. *Mol. Cryst. Liq. Cryst.* **1995**, *274*, 167.
(54) Aubin, S. M. J.; Spagna, S.; Eppley, H. J.; Sager, R. E.; Folting, K.; Christou, G.; Hendrickson, D. N. *Mol. Cryst. Liq. Cryst.* **1997**, *305*, 181.
(55) Eppley, H. J.; Aubin, S. M. J.; Wemple, M. W.; Adams, D. M.; Tsai, H.-L.; Grillo, V. A.; Castro, S. L.; Sun, Z.; Folting, K.; Huffman, J. C.; Hendrickson, D. N.; Christou, G. *Mol. Cryst. Liq. Cryst.* **1997**, *305*, 167.
(56) Schake, A. R.; Tsai, H.-L.; de Vries, N.; Webb, R. J.; Folting, K.; Hendrickson, D. N.; Christou, G. *Chem. Commun.* **1992**, 181.
(57) Sessoli, R.; Tsai, H.-L.; Schake, A. R.; Wang, S.; Vincent, J. B.; Folting, K.; Gatteschi, D.; Christou, G.; Hendrickson, D. N. *J. Am. Chem. Soc.* **1993**, *115*, 1804.
(58) Ruiz, D.; Sun, Z.; Albela, B.; Folting, K.; Ribas, J.; Christou, G.; Hendrickson, D. N. *Angew. Chem., Int. Ed. Engl.* **1998**, *37*, 300.
(59) Aubin, S. M. J.; Sun, Z.; Guzei, I. A.; Rheingold, A. L.; Christou, G.; Hendrickson, D. N. *Chem. Commun.* **1997**, 2239.
(60) Sun, Z.; Ruiz, D.; Rumberger, E.; Incarvito, C. D.; Folting, K.; Rheingold, A. L.; Christou, G.; Hendrickson, D. N. *Inorg. Chem.* **1998**, *37*, 4758.
(61) Sun, Z.; Ruiz, D.; Dilley, N. R.; Soler, M.; Ribas, J.; Guzei, I. A.; Rheingold, A. L.; Folting, K.; Maple, M. B.; Christou, G.; Hendrickson, D. N. *Chem. Commun.* **1999**, 1973.
(62) Eppley, H. J.; Tsai, H.-L.; de Vries, N.; Folting, K.; Christou, G.; Hendrickson, D. N. *J. Am. Chem. Soc.* **1995**, *117*, 301.
(63) Aubin, S. M. J.; Spagna, S.; Eppley, H. J.; Sager, R. E.; Christou, G.; Hendrickson, D. N. *Chem. Commun.* **1998**, 803.

cubane core $[Mn^{IV}Mn^{III}_3O_3X]^{6+}$,[65,66] and an iron complex of the form $[Fe_4(OCH_3)_6(dpm)_6]$, where dpm^- is the anion of the ligand dipivaloylmethane.[67] Finally, the octanuclear iron complex, $[Fe_8O_2(OH)_{12}(tacn)_6]^{8+}$, where tacn is for the ligand triazacyclononane, has also been shown to be an SMM.[68]

In our efforts to find new examples of SMM's, we very recently characterized a new manganese based SMM with the chemical composition $[Mn_4(pdmH)_6(O_2CCH_3)_2](ClO_4)_2$ (**1**),[69] incorporating the monodeprotonated anion of the ligand pyridine dimethanol ($pdmH^-$). The magnetic properties of this complex were fully characterized by DC and AC magnetic susceptibility and by high-frequency EPR (HFEPR) measurements. The hydrated form of complex **1** (**1**·$2.5H_2O$) was determined by HFEPR to have a ground-state spin of $S = 9$ and axial zero-field splitting parameter of $D/k_B = -0.45$ K, giving it a barrier for the reversal of magnetization of 36.5 K. Frequency-dependent, out-of-phase AC magnetic susceptibility signals in the 2 K region were seen. A temperature-independent magnetization relaxation time on the order of 10^4 seconds was observed below 1 K.[70] This was attributed to quantum mechanical tunneling of the direction of magnetization between the lowest M_s components of the ground state. This is a significant observation that adds to our understanding of magnetization relaxation in SMM's.

We herein present results on our latest efforts in the discovery of new SMM's. Two new tetranuclear mixed-valence manganese complexes were isolated using the following ligands similar to $pdmH^-$:

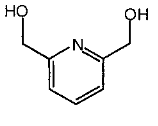

pdmH$_2$

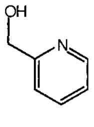

hmpH

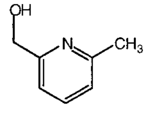

6-Me-hmpH

With hmpH, the complex $[Mn_4(hmp)_6Br_2(H_2O)_2]Br_2$ **(2)** was isolated, whereas with 6-me-hmpH, the structurally different complex $[Mn_4(6\text{-}me\text{-}hmp)_6Cl_4]$ **(3)** was characterized.

Experimental Section

Synthesis. All manipulations were carried out under aerobic conditions using commercial grade solvents. Manganous chloride, manganous bromide, 2-hydroxymethyl-pyridine (pyridyl-carbinol, Aldrich), 6-methyl-2-hydroxymethylpyridine (Aldrich), and tetraethylammonium hydroxide were all used as received without further purification. Tetrabutylammonium permanganate was prepared as described elsewhere.[71]

Table 1. Crystallographic Data for $[Mn_4(hmp)_6Br_2(H_2O)_2]Br_2 \cdot 4H_2O$ (**2**) and $[Mn_4(6me\text{-}hmp)_6Cl_4] \cdot 4H_2O$(**3**)

	(**2**)	(**3**)
formula	$C_{36}H_{48}Br_4Mn_4N_6O_{12}$	$C_{42}H_{56}Cl_4Mn_4N_6O_{10}$
a, Å	10.907(0)	17.0852(4)
b, Å	15.788(0)	20.8781(5)
c, Å	13.941(0)	14.1835(3)
α, (deg)	90	90
β, (deg)	101.21(0)	90.5485(8)
γ, (deg)	90	90
V, Å^3	2354.94	5059.1
Z	2	4
formula weight	1296.18 g mol^{-1}	1166.50 g mol^{-1}
space group	$P21/c$	$C2/c$
T, °C	−160	−160
λ, Å	0.71069[a]	0.71073[a]
ρ_{cald}, g/cm^{-3}	1.828	1.532
μ(Mo Kα), cm^{-1}	45.142	12.450
R[b]	0.030	0.038
R_w[c]	0.025	0.043

[a] Graphite monochromator. [b] $R = \sum[|F_o| - |F_c|]/\sum|F_o|$. [c] $R_w = [\sum w(|F_o| - |F_c|)^2/\sum w|F_o|^2]$, where $w = 1/\sigma^2(|F_o|)$.

$[Mn_4(hmp)_6Br_2(H_2O)_2]Br_2$ (2). A total of 376 mg of 2-hydroxymethylpyridine (hmpH) and 395 mg of $MnBr_2 \cdot 4H_2O$ were dissolved in 20 mL of MeCN. To this was added 530 mg of a 20wt % water solution of tetraethylammonium hydroxide. The solution turned red-brown and this was stirred for 40−60 min and then filtered. The filtrate was then left to slowly evaporate. Dark cubelike crystals formed in 1−2 weeks. Anal. Calc (Found) for $C_{36}H_{48}Br_4Mn_4N_6O_{12}$: C, 33.36 (33.83); H, 3.73 (3.47); N, 6.48 (6.56). Selected IR data (cm^{-1}): 3350.2 (br), 1604.7 (s), 1483.2 (m), 1438.8 (m), 1282.6 (w), 1226.7 (w), 1155.3 (w), 1045.4 (s), 765.7 (s), 659.6 (s), 567.1 (s).

$[Mn_4(6\text{-}me\text{-}hmp)_6Cl_4] \cdot 4H_2O$ (3). 432 mg of 6-methyl-2-hydroxymethylpyridine (6me-hmp) and 273 mg of $MnCl_2 \cdot 4H_2O$ were dissolved in 20 mL of MeOH. To this was added in portions 125 mg of tetrabutylammonium permanganate. The solution turned an intense brown color. This solution was stirred for 1 h. An equal volume of MeCN was added and the mixture was left to slowly evaporate. Dark prism-shaped crystals formed over several days. Anal. Calc (Found) for $C_{42}H_{56}Cl_4Mn_4N_6O_{10}$: C, 43.25 (43.26); H, 4.84 (4.70); N, 7.20 (7.43). Selected IR data (cm^{-1}): 3506.4 (br), 1606.6 (m), 1465.8 (m), 1359.8 (m), 1222.8 (w), 1170.7 (w), 1082 (s), 781.1 (m), 680.3 (m), 572.8 (m), 430.2 (w).

X-ray Crystallography. A suitable crystal was affixed to the end of a glass fiber using silicone grease and rapidly transferred to the goniostat where it was cooled for characterization and data collection. X-ray crystallographic data were collected on a Picker four-circle diffractometer at −160 °C. Details of the diffractometry, low-temperature facilities, and computational procedures employed by the Molecular Structure Center are available elsewhere.[72] The structure was solved by direct methods (SHELXTL) and Fourier methods and refined on F by full-matrix least-squares cycles.

For complex **2**·$4H_2O$, a systematic search of a limited hemisphere of reciprocal space revealed monoclinic symmetry and systematic absences corresponding to the unique space group $P2_1/c$. After data collection ($+h, \pm k, \pm l$; $6° < 2\theta < 50°$) and processing, and averaging of reflections measured more than once ($R_{av} = 0.198$), the structure was solved without serious problems. The Mn_4 cation lies at a center of inversion. In the final refinement cycles, non-hydrogen atoms were refined anisotropically. Hydrogen atoms were included for the cation in fixed, idealized positions with thermal parameters of 1.0 plus the isotropic thermal parameter of the parent atom. Final R and R_w values are listed in Table 1.

---

(64) (a) Sun, Z.; Castro, S. L.; Bollinger, J. C.; Hendrickson, D. N.; Christou, G. *Chem. Commun.* **1995**, 2517. (b) Castro, S. L.; Sun, Z.; Grant, C. M.; Bollinger, J. C.; Hendrickson, D. N.; Christou, G. *J. Am. Chem. Soc.* **1998**, *120*, 2365.

(65) Aubin, S. M. J.; Wemple, M. W.; Adams, D. M.; Tsai, H.-L.; Christou, G.; Hendrickson, D. N. *J. Am. Chem. Soc.* **1996**, *118*, 7746.

(66) (a) Aubin, S. M. J.; Dilley, N. R.; Wemple, M. W.; Maple, M. B.; Christou, G.; Hendrickson, D. N. *J. Am. Chem. Soc.* **1998**, *120*, 839. (b) Aubin, S. M. J.; Dilley, N. R.; Pardi, L.; Krzystek, J.; Wemple, M. W.; Brunel, L.-C.; Maple, M. B.; Christou, G.; Hendrickson, D. N. *J. Am. Chem. Soc.* **1998**, *120*, 4991.

(67) Barra, A. L.; Caneschi, A.; Cornia, A.; Fabrizi de Biani, F.; Gatteschi, D.; Sangregorio, C.; Sessoli, R.; Sorace, L. *J. Am. Chem. Soc.* **1999**, *121*, 5302.

(68) Barra, A.-L.; Debrunner, P.; Gatteschi, D.; Schulz, Ch. E.; Sessoli, R. *Europhys. Lett.* **1996**, *35*, 133.

(69) (a) Brechin, E. K.; Yoo, J.; Nakano, M.; Huffman, J. C.; Hendrickson, D. N. Christou, G. *Chem. Commun.* **1999**, 783. (b) Yoo, J.; Brechin, E. K.; Yamaguchi, A.; Nakano, M.; Huffman, J. C.; Maniero, A. L.; Brunel, L.-C.; Awaga, K.; Ishimoto, H.; Christou, G.; Hendrickson, D. N. *Inorg. Chem.* **2000**, *39*, 3615.

(70) Yamaguchi, A.; Ishimoto, H.; Awaga, K.; Yoo, J.; Nakano, M.; Hendrickson, D. N.; Brechin, E. K.; Christou, G. *Physica B* **2000**, *284*, 1225.

(71) Vincent, J. B.; Chang, H.-R.; Folting, K.; Huffman, J. C.; Christou, G.; Hendrickson, D. N. *J. Am. Chem. Soc.* **1987**, *109*, 5703.

(72) Chisholm, M. H.; Folting, K.; Huffman, J. C.; Kirkpatrick, C. C. *Inorg. Chem.* **1984**, *23*, 1021.

For complex $\mathbf{3}\cdot 4H_2O$, a systematic search of a limited hemisphere of reciprocal space revealed monoclinic symmetry and systematic absences corresponding to one of the monoclinic space groups, *C*2/*c* or *Cc*. Subsequent solution and refinement of the structure confirmed centrosymmetric *C*2/*c* to be the correct space group. All non-hydrogen atoms were readily located and refined anisotropically; hydrogen atoms were included in calculated positions as fixed atom contributors in the final refinement cycles. Final R and R_w values are listed in Table 1.

Physical Methods. IR measurements were made on samples pressed into KBr pellets using a Nicolet Magna-IR 550 spectrophotometer. DC magnetic susceptibility experiments were performed on powdered microcrystalline samples (restrained in eicosane to prevent torquing at high fields) with a Quantum Design MPMS5 SQUID magnetometer equipped with a 5.5 T (55 kG) magnet and capable of operating in the 1.7−400 K range. Diamagnetic contributions to the susceptibility were corrected using Pascal's constants. AC magnetic susceptibility experiments above 1.7 K were carried out on a Quantum Design MPMS2 SQUID magnetometer. AC field strength can be varied from 0.5 to 5 G at frequencies ranging from 0.01 to 1000 Hz. The temperature range available is 1.7 to 400 K. Low-temperature AC magnetic susceptibility experiments down to the millikelvin temperature range were performed at the Institute of Solid State Physics, The University of Tokyo. Details of the measurement and the experimental set up are described elsewhere.[69b]

High-frequency and -field EPR spectra were recorded at the National High Magnetic Field Laboratory, Tallahassee, Florida. The spectrometer is described in detail elsewhere[73] and is equipped with a 15/17 T superconducting magnet and can achieve temperatures ranging from 4 to 300 K. In this work, a Gunn diode operating at a fundamental frequency of 95 ± 3 GHz was used. The operating frequency range is 95−490 GHz. Frequencies between ca. 180 and 490 GHz were obtained by using a solid-state harmonic generator that multiplies the fundamental frequency (i.e., 95 GHz) and high pass filters to filter out the lower frequency harmonics, however, the higher frequency harmonics pass through. The magnetic field was modulated at a typical frequency of 8.5 kHz and amplitude of 1.5 mT for the purpose of phase-sensitive detection. The magnetic field was swept at a rate of 0.2 T/min over a 0−14.5 T range.

Results and Discussion

Synthesis. Nitrogen−oxygen containing chelates such as picolinic acid, 2-hydroxymethyl-pyridine, 2-hydroxyethyl-pyridine, and pyridine-2,6-dimethanol are known to stabilize polynuclear manganese complexes with nuclearities of four,[69,74] seven,[75] and eighteen.[76] Recently, we reported a new structural type of a polynuclear manganese complex $[Mn_4(pdmH)_6(O_2CCH_3)_2](ClO_4)_2$ (**1**) which was obtained in the reaction of monoanionic pyridine-2,6-dimethanol ($pdmH^-$) with a μ_3-oxo-bridged trinuclear manganese carboxylate complex.[69] The complex was structurally determined to be tetranuclear with 2 Mn^{II} and 2 Mn^{III} ions. Unlike previously characterized tetranuclear Mn complexes,[74] the bridging is derived from the oxygen atom of the ligand; no bridging oxides are present as found in most polynuclear Mn complexes. The magnetic properties of this complex were fully characterized employing the DC and AC magnetic susceptibility and HFEPR techniques. It was found to be a new example of a SMM.

It was reasoned that a family of this structural type could be found through the use of similar nitrogen−oxygen containing chelates such as 2-hydroxymethyl-pyridine (hmpH) and 6-methyl-2-hydroxymethyl-pyridine (6-me-hmpH), ligands with only one methanolic substituent on the pyridine ring in contrast to the two on the $pdmH^-$ ligand. Initially, parallel reactions using hmpH instead of $pdmH_2$ with the trinuclear manganese carboxylate source produced a decanuclear manganese complex.[77] Thus, other routes were tried and it was found that reactions using simple mononuclear manganese complexes such as $MnCl_2$ or $MnBr_2$ in the presence of hmpH produced discrete tetranuclear complexes. It was concluded that the two new complexes resemble complex **1** based on initial IR data, but the structures were confirmed by X-ray crystallography.

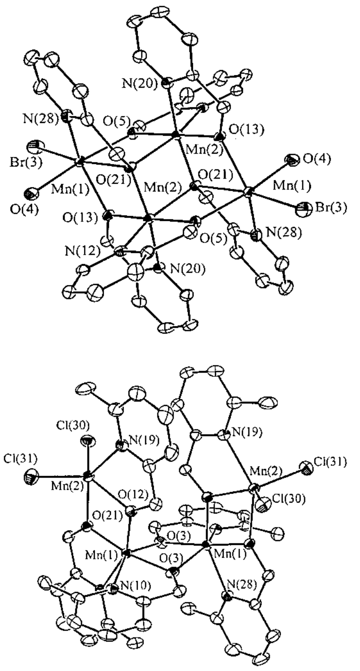

Figure 2. ORTEP representation of the cation of complex **2**, $[Mn_4(hmp)_6Br_2(H_2O)_2]Br_2\cdot 4H_2O$ (top), and complex **3**, $[Mn_4(6me\text{-}hmp)_6Cl_4]\cdot 4H_2O$ (bottom).

Descriptions of Structures. Labeled ORTEP plots of the cation of $[Mn_4(hmp)_6Br_2(H_2O)_2]Br_2\cdot 4H_2O$ **(2)** and $[Mn_4(6me\text{-}hmp)_6Cl_4]\cdot 4H_2O$ **(3)** are given in Figure 2 and selected interatomic distances and angles are listed in Tables2 and 3, respectively. Complex $\mathbf{2}\cdot 4H_2O$ crystallizes in the monoclinic space group $P2_1$/c with the cation lying on an inversion center and consisting of a planar Mn_4 rhombus. The unit cell contains 2 Br^- counterions and 4 solvate water molecules per Mn_4 unit. Complex **2** is mixed-valence consisting of 2 Mn^{II} and 2 Mn^{III} ions and is similar to the tetranuclear manganese complex containing the ligand $pdmH^-$, complex **1**, with two exceptions. Unlike **1** which has acetates as additional bridging ligands, the monoanionic bidentate 2-hydroxymethylpyridine (hmp^-) ligand serves as the only bridging ligand in complex **2**. In addition, all the Mn atoms in complex **2** have hexacoordinate geometry, whereas, two of the Mn atoms (Mn^{II}) are heptacoordinate in complex **1**. The Mn_4 rhombus in complex **2** is composed of two Mn_3 triangular faces held together by a μ_3-oxygen atom [O(21)] of hmp^-. The edges of each triangular face consists of a μ_2-oxygen atoms [O(13)] and [O(5)]. Mn(1) and Mn(2) are assigned as the Mn^{II} and Mn^{III} ions, respectively, on the basis of bond valence sum calculations and the presence at Mn(2) of a Jahn−Teller elongation axis [O(21)−Mn(2)−N(12)].

---

(73) Hassan, A. K.; Pardi, L. A.; Krzystek, J.; Sienkiewica, A.; Goy, P.; Rohrer, M.; Brunel, L.-C. *J. Magn. Reson.* **2000**, *142*, 300.

(74) (a) Libby, E.; McCusker, J. K.; Schmitt, E. A.; Folting, K.; Hendrickson, D. N.; Christou, G. *Inorg. Chem.* **1991**, *30*, 3486. (b) Bouwmann, E.; Bolcar, M. A.; Libby, E.; Huffman, J. C.; Folting, K.; Christou, G. **1992**, *31*, 5185.

(75) Bolcar, M. A.; Aubin, S. M. J.; Folting, K.; Hendrickson, D. N.; Christou, G. *J. Chem. Soc., Chem. Commun.* **1997**, 1485.

(76) Brechin, E. K.; Yoo, J.; Bolcar, M. A.; Hendrickson, D. N.; Christou, G. Unpublished results.

(77) Aromi, G.; Aubin, S. M. J.; Bolcar, M, A.; Christou, G.; Eppley, H. J.; Folting, K.; Hendrickson, D. N.; Huffman, J. C.; Squire, R. C.; Tsai, H.-L.; Wang, S.; Wemple, M. W. *Polyhedron* **1998**, *17*, 3005.

Table 2. Selected Interatomic Distances (Å) and Angles (deg) for $[Mn_4(hmp)_6Br_2(H_2O)_2]Br_2{\cdot}4H_2O$

Mn(1)	O(4)	2.226(2)	Mn(2)	O(5)	1.8882(17)
Mn(1)	O(5)	2.1950(18)	Mn(2)	O(13)	1.8770(17)
Mn(1)	O(13)	2.1477(18)	Mn(2)	O(21)	1.9545(18)
Mn(1)	O(21)	2.2952(17)	Mn(2)	O(21)	2.2563(18)
Mn(1)	N(28)	2.235(2)	Mn(2)	N(12)	2.217(2)
Mn(1)	Br(3)	2.554	Mn(2)	N(20)	2.048(2)

O(4)	Mn(1)	O(5)	168.89(8)	O(5)	Mn(2)	N(20)	97.54(8)
O(4)	Mn(1)	O(13)	83.66(9)	O(13)	Mn(2)	O(21)	83.51(8)
O(4)	Mn(1)	O(21)	95.71(8)	O(13)	Mn(2)	O(21)	95.75(8)
O(4)	Mn(1)	N(28)	83.33(9)	O(13)	Mn(2)	N(12)	106.07(8)
O(4)	Mn(1)	Br(3)	94.61(0)	O(13)	Mn(2)	N(20)	80.66(8)
O(5)	Mn(1)	O(13)	92.02(7)	O(21)	Mn(2)	O(21)	81.65(7)
O(5)	Mn(1)	O(21)	73.18(6)	O(21)	Mn(2)	N(12)	97.67(8)
O(5)	Mn(1)	N(28)	93.48(8)	O(21)	Mn(2)	N(12)	157.99(7)
O(5)	Mn(1)	Br(3)	96.49(0)	O(21)	Mn(2)	N(20)	163.53(8)
O(13)	Mn(1)	O(21)	70.03(6)	O(21)	Mn(2)	N(20)	95.39(8)
O(13)	Mn(1)	N(28)	139.34(8)	N(12)	Mn(2)	N(20)	91.08(9)
O(13)	Mn(1)	Br(3)	113.39(0)	Mn(1)	O(5)	Mn(2)	119.19(8)
O(21)	Mn(1)	N(28)	73.18(7)	Mn(1)	O(13)	Mn(2)	107.24(8)
O(5)	Mn(2)	O(13)	175.21(8)	Mn(1)	O(21)	Mn(2)	95.66(6)
O(5)	Mn(2)	O(21)	97.88(8)	Mn(1)	O(21)	Mn(2)	99.22(8)
O(5)	Mn(2)	O(21)	79.96(7)	Mn(1)	O(21)	Mn(2)	98.35(7)
O(5)	Mn(2)	N(12)	78.34(8)				

Table 3. Selected Interatomic Distances (Å) and Angles (deg) for $Mn_4(6me\text{-}hmp)_6Cl_4]{\cdot}4H_2O$

Mn(1)	O(3)	1.909(2)	Mn(2)	Cl(30)	2.3782(9)
Mn(1)	O(3)	2.194(2)	Mn(2)	Cl(31)	2.3768(10)
Mn(1)	O(12)	1.919(2)	Mn(2)	O(12)	2.092(2)
Mn(1)	O(21)	1.867(2)	MN(2)	O(21)	2.184(2)
Mn(1)	N(10)	2.264(3)	Mn(2)	N(19)	2.288(3)
Mn(1)	N(28)	2.146(3)			

O(3)	Mn(1)	O(3)	74.18(9)	O(21)	Mn(1)	N(28)	80.28(1)
O(3)	Mn(1)	O(12)	104.32(9)	N(10)	Mn(1)	N(28)	89.94(10)
O(3)	Mn(1)	O(12)	94.34(9)	Cl(30)	Mn(2)	Cl(31)	115.35(4)
O(3)	Mn(1)	O(21)	98.95(9)	Cl(30)	Mn(2)	O(12)	125.47(7)
O(3)	Mn(1)	O(21)	168.54(10)	Cl(30)	Mn(2)	O(21)	94.98(6)
O(3)	Mn(1)	N(10)	148.54(9)	Cl(30)	Mn(2)	N(19)	107.06(7)
O(3)	Mn(1)	N(10)	77.49(9)	Cl(31)	Mn(2)	O(12)	118.91(7)
O(3)	Mn(1)	N(28)	86.02(9)	Cl(31)	Mn(2)	O(21)	103.59(7)
O(3)	Mn(1)	N(28)	107.93(10)	Cl(31)	Mn(2)	N(19)	95.27(8)
O(12)	Mn(1)	O(21)	78.28(9)	O(12)	Mn(2)	O(21)	67.92(8)
O(12)	Mn(1)	N(10)	91.09(9)	O(12)	Mn(2)	N(19)	73.41(9)
O(12)	Mn(1)	N(29)	157.38(10)	O(21)	Mn(2)	N(19)	141.32(9)
O(21)	MN(1)	N(10)	111.09(10)	Mn(1)	O(3)	Mn(1)	102.43(9)
Mn(1)	O(12)	Mn(2)	107.75(10)	Mn(1)	O(21)	Mn(2)	106.04(10)

The analysis of the X-ray data shows closely positioned Mn_4 clusters in the unit cell. The closest internuclear distance between the coordinated Br anions of the Mn_4 cluster is 4.91 Å. In addition to coordinated Br atoms, there are Br counterions very near the Mn_4 molecule. The closest separation between a Br counterion and the coordinated Br of a Mn_4 complex is 5.25 Å. There are also 4 closely positioned water molecules per Mn_4 molecule in the unit cell. The distance between a water molecule and a coordinated Br is 2.76 Å. Water molecules are also in close proximity to a coordinated water of a Mn_4 complex. The oxygen−oxygen distance between a solvate water and a coordinated water is 3.49 Å. The 2.76 and 3.49 Å separations are well within the range for hydrogen bonding. Thus, from the manner in which the Mn_4 molecules are packed crystallographically, intermolecular interactions between neighboring Mn_4 molecules may be appreciable.

Careful analysis of the X-ray data also reveals that the Jahn−Teller axis [O(21)−Mn(2)−N(12)] is slightly bent. The angle formed by the O(21)−Mn(2) and the Mn(2)−N(12) bonds is 158° and not the 180° expected. In addition, two of the Mn_4 molecules in the unit cell are mutually related by a glide plane. The result is that the easy axes of two of the Mn_4 clusters in the unit cell of complex **2** are not exactly parallel. The angle between the two molecular easy axes is close to 9.0 ± 0.5°. This slight canting of the easy molecular axis is important to consider in the analysis of HFEPR data.

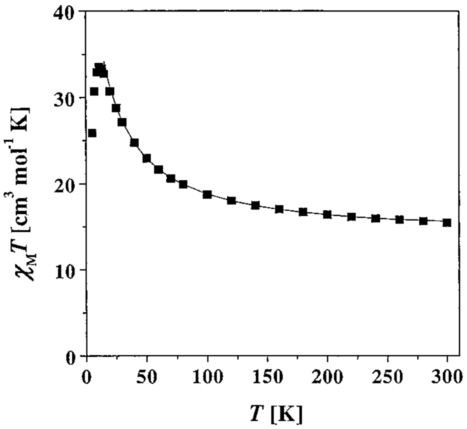

Figure 3. Plot of $\chi_M T$ vs temperature for a microcrystalline sample of complex **2** restrained in eicosane. The susceptibility, χ_M, was measured under a 10 kG magnetic field with the sample restrained in eicosane. The solid line corresponds to the fit of the data as described in the text.

Complex $\mathbf{3}{\cdot}4H_2O$ crystallizes in a monoclinic space group *C*2/*c* and is best described as having four manganese ions arranged in a bent chain. The complex is also mixed-valence containing 2 Mn^{II} ions and 2 Mn^{III} ions but has no counterions as the charge is balanced by the coordinated ligands. Bridging between the metal centers is accomplished by the μ_2-oxygen of the 6-methyl-2-hydroxymethylpyridine anionic ligand; the chloride ions are terminal and are only bonded to the outer Mn ions of the chain. The two outer Mn ions are pentacoordinate and the two inner Mn ions are hexacoordinate. The inner two Mn ions, Mn(1), are identified as being Mn^{III} based on bond valence sum calculations and the presence of a Jahn−Teller elongation axis [O(3)−Mn(1)−N(10)]. There are 4 solvate molecules per molecule of complex **3** in the crystal. The closest contact made between a solvate water molecule and a Mn_4 unit is 3.2 Å. The Mn_4 unit of complex **3** is also tightly packed in a rowlike fashion. There are close van der Waal contacts (3.5−4.2 Å) between the pyridine rings of the 6-me-hmp$^-$ ligand of neighboring Mn_4 complexes. Thus, it is possible that there are intermolecular interactions between molecules of complex **3**. No canting of the easy molecular axes is observed between molecules of complex **3**.

DC Magnetic Susceptibility. Variable temperature magnetic susceptibility measurements were carried out on microcrystalline samples of **2** and **3** restrained in eicosane. The data were collected with a 10 kG applied magnetic field in the 5−300 K range. Figure 3 shows the data plotted as $\chi_M T$ vs temperature for complex **2**. The magnetic properties of **2** are similar to those observed for ferromagnetically coupled alkoxide bridged complexes[78] and the hydrated form of complex **1**.[69b] In fact, the $\chi_M T$ vs T plot of complex **2** was found to be virtually superimposable to that of $\mathbf{1}{\cdot}2.5H_2O$. As shown in Figure 3, the value of $\chi_M T$ increases from 15.5 cm^3 mol^{-1} K (spin only ∼14.75 cm^3 mol^{-1} K) at room temperature to a maximum of 33.6 cm^3 mol^{-1} K at 11 K and then decreases slightly to 25.9 cm^3 mol^{-1} K at 5 K. Ferromagnetic interactions are the dominant

---

[78] (a) Schake, A. R.; Schmitt, E. A.; Conti, A. J.; Streib, W. E.; Huffman, J. C.; Hendrickson, D. N.; Christou, G. *Inorg. Chem.* **1991**, *30*, 3192. (b) Gelasco, A.; Kirk, M. L.; Kampf, J. W.; Pecoraro, V. L. *Inorg. Chem.* **1997**, *36*, 1829.

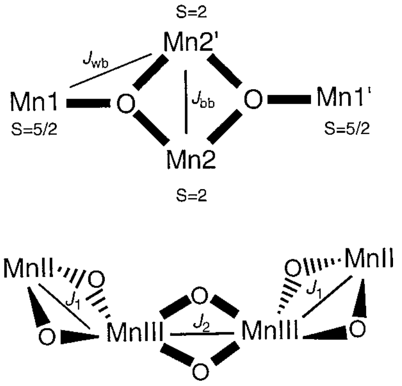

Figure 4. Diagram showing the two dominant magnetic exchange pathways between metal centers in complex **2** (top) and complex **3** (bottom).

interactions as indicated by the increase in the value of $\chi_M T$ with decreasing temperature and are the origin of the high spin ground state of complex **2**. The small decrease in $\chi_M T$ at lowest temperatures is likely the result of magnetization saturation in a 10 kG magnetic field, intermolecular interactions, or zero-field splitting in the ground state.

The $\chi_M T$ vs temperature data for complex **2** were fit in order to determine the magnitudes of the ferromagnetic exchange interactions. It was expected that the ferromagnetic interactions in complex **2** would be nearly identical to that found for complex **1**$\cdot 2.5H_2O$. The same procedure used to fit the data for **1**$\cdot 2.5H_2O$ was used to fit the data shown in Figure 3. Because of the near identical core structure between complex **2** and **1**$\cdot 2.5H_2O$, a model which considers only two dominant exchange pathways was used as shown in Figure 4 (top). This approximation equates $J_{1'2} = J_{1'2'} = J_{12} = J_{12'} = J_{wb}$ and the Kambe vector coupling method can be used to solve the spin Hamiltonian which is given in eq 1:

$$\hat{H} = -J_{wb}(\hat{S}_T^2 - \hat{S}_A^2 - \hat{S}_B^2) - J_{bb}(\hat{S}_A^2 - \hat{S}_1^2 - \hat{S}_3^2) \quad (1)$$

where: $\hat{S}_A = \hat{S}_1 + \hat{S}_3$, $\hat{S}_B = \hat{S}_2 + \hat{S}_4$, and $\hat{S}_T = \hat{S}_A + \hat{S}_B$. The Kambe method gives the eigenvalue expression in eq 2:

$$E(S_T) = -J_{wb}[S_T(S_T + 1) - S_A(S_A + 1) - S_B(S_B + 1)] - J_{bb}[S_A(S_A + 1)] \quad (2)$$

With two $S = 2$ [Mn(III)] and two $S = 5/2$ [Mn(II)] interacting ions present in complex **2** there are a total of 110 possible states with S_T, the total spin of the Mn_4 complex, ranging from 0 to 9. A list of all these 110 different spin states with their S_T, S_A and S_B values is available in the Supporting Information.

$$\chi_M = \left(\frac{Ng^2\mu_B^2}{3kT}\right)\frac{\sum[S_T(S_T + 1)(2S_T + 1)]e^{-E(S_T)/k_BT}}{\sum(2S_T + 1)e^{-E(S_T)/k_BT}} + \mathrm{TIP} \quad (3)$$

This eigenvalue expression eq 2 and the corresponding Van Vleck eq 3 were then used to least-squares fit the experimental data measured in the 5−300 K range (Figure 3). Data below 15 K were omitted in the fitting because zero-field and magnetization saturation effects are likely to influence the data in this temperature range. The parameters g, J_{wb} and J_{bb} were varied to fit the data. At each setting of the parameters eq 2 is used to calculate the energy for each of the 110 spin states and then these energies are used in eq 3 to calculate the molar paramagnetic susceptibility. The three parameters are varied until a good fit to the experimental susceptibility is found. With the temperature independent paramagnetism (TIP) fixed at 600×10^{-6} cm^3 mol^{-1}, a good fit was achieved (solid line, Figure 3) with the fitting parameters $g = 1.94$, $J_{wb}/k_B = 1.34$ K, and $J_{bb}/k_B = 12.65$ K. These values correspond to a ground state with $(S_T, S_A, S_B) = (9, 4, 5)$. It must be emphasized that the magnitudes of the exchange interactions in complex **2** are comparable to those found for complex **1**$\cdot 2.5H_2O$ which also has a ground state with $S = 9$.[69b]

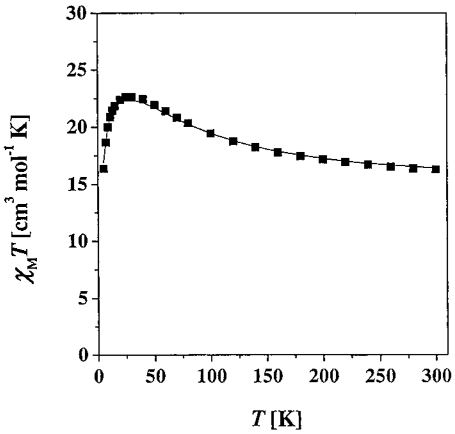

Figure 5. Plot of $\chi_M T$ vs temperature for a microcrystalline sample of complex **3** restrained in eicosane. The susceptibility, χ_M, was measured under a 10 kG magnetic field with the sample restrained in eicosane. The solid line corresponds to the fit of the data as described in the text.

The variable temperature susceptibility data for complex **3** also show signs of ferromagnetic interactions. Figure 5 gives the data plotted as $\chi_M T$ vs temperature. The value of $\chi_M T$ increases from 16.3 cm^3 mol^{-1} K at 300 K to around 22.6 cm^3 mol^{-1} K at 30 K before decreasing to 16.4 cm^3 mol^{-1} K at 5 K. Compared to the data for complex **2**, a broader maximum is observed at low temperatures in the plot of $\chi_M T$ vs temperature for complex **3**. In addition, the increase in $\chi_M T$ at low temperatures is not as dramatic as seen for complex **2** resulting in a lower value of $\chi_M T$ at the peak. It is likely that the magnetic exchange interactions in complex **3** are different from those in complex **2**. However, the increase in $\chi_M T$ at low temperatures suggests that the magnetic exchange interactions are dominantly ferromagnetic. Magnetization saturation, intermolecular interaction, or zero-field splitting in complex **3** is likely the origin of the decrease in $\chi_M T$ at low temperatures.

It can be seen in the diagram in Figure 4 (bottom) that there are only two different exchange pathways in complex **3**. The two terminal $Mn^{II}-Mn^{III}$ interactions are equivalent from symmetry considerations. However, the Kambe vector-coupling method cannot be employed to analyze the variable-temperature susceptibility data for complex **3**. The analysis of these data will be described in the next section.

Variable-Field DC Magnetization Measurements. The nature of the ground states and zero-field splittings of complexes **2** and **3** were further examined through variable field magnetization measurements. Saturation of magnetization is achieved at high fields and low temperatures; the field dependence of the magnetization can be analyzed to obtain the spin of the ground state (=S) and the magnitude of the zero-field splitting. At high fields and low temperatures, a true powder average of the theoretically calculated magnetization for all orientations

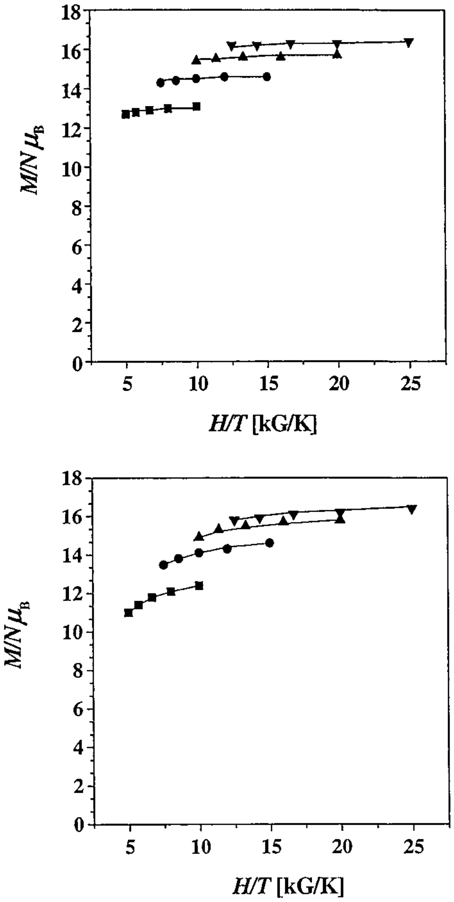

Figure 6. Plot of the reduced magnetizaton $M/N\mu_B$ vs the ratio of external field and the absolute temperature [kG/K]. Data for complex **2** (top) and complex **3** (bottom) were measured at 20 (■), 30(●), 40 (▲), and 50 (▼) kG in the 2−4 K range. The solid lines correspond to the fits (see text).

must be made[79] using eq 4. In eq 4 θ and ϕ are the polar angle orientations of the field with respect to the molecular principal

$$\bar{M} = \frac{-N}{4\pi}\int_{\theta=0}^{\pi}\int_{\theta=0}^{2\pi}\left[\sum_{i=1}^{p}\left(\frac{\delta E_i}{\delta H}\right)\exp(-E_i/kT)/\sum_{i=1}^{p}\exp(-E_i/kT)\right]\sin\theta \, d\,\theta \text{Ø} \quad (4)$$

axis system and $\delta E_i/\delta H$ is the change in the energy of the *i*th level in response to a change in a magnetic field. The energies of the various sublevels of the ground state are obtained by diagonalization of the $(2S + 1) \times (2S + 1)$ Hamiltonian matrix which includes the Zeeman terms. The derivatives $\delta E_i/\delta H$ were calculated from the corresponding eigenvectors with the Hellmann−Feynman theorem[79] The integral in eq 4 was evaluated numerically. For complexes with no zero-field splitting, the plot of magnetization versus external magnetic field follows a simple Brillouin function where the magnetization saturates at a value of gS and the isofield lines are superimposed. Magnetization measurements were carried out for complexes **2** and **3** in 20−50 kG fields and in the 2.0−4.0 K range. The results for complex **2** (top) and complex **3** (bottom) are plotted as reduced magnetization $M/N\mu_B$ vs H/T in Figure 6, where M is the magnetization, N is Avogadro's number, μ_B is the Bohr magneton, and H is the magnetic field. It is apparent that complexes **2** and **3** both have ground states under these conditions that have a large spin and appreciable zero-field splitting. At the highest field and lowest temperature complexes **2** and **3** have saturation of magnetization values of 16.40 $N\mu_B$ and 16.45 $N\mu_B$, respectively. Zero-field splitting is evident by the nonsuperposition of the isofield lines. The saturation of magnetization value of 16.4 $N\mu_B$ for complex **2** is similar to that observed for complex **1**·2.5H$_2$O, which was determined to have a ground-state spin of $S = 9$. The saturation value of 16.45 $N\mu_B$ for complex **3** seems to suggest that it also has a ground state of $S = 9$.

The variable field magnetization data for complexes **2** and **3** were analyzed to determine the spin of the ground state (S) and the D values. For complex **2**, the data sets were fit using a model which assumes that the ground state is well-isolated and is the only state populated in the 2−4 K and 20−50 kG ranges. A spin Hamiltonian including the Zeeman interaction and axial zero-field spitting ($D\hat{S}_Z^2$) was used to least-squares fit the data. The results of the fitting are shown as solid lines in Figure 6. The fitting of the data assuming a $S = 9$ ground state produced nearly the same g and D parameters as were obtained for **1**·2.5H$_2$O.[69b] The fit of the data for complex **2** gave $g = 1.95$ and $D/k_B = -0.34$ K as the final optimized parameters for a spin ground state of $S = 9$.

For complex **3**, it was not possible to accurately fit the experimental data accounting for only the Zeeman and axial zero-field splitting terms. It was concluded that in addition to the ground-state one or more excited states are populated under the experimental conditions. Thus, a full Hamiltonian matrix diagonalization approach was taken where the data were nonlinear least-squares fit using a downhill simplex method. The spin Hamiltonian used is shown in eq 5:

$$\hat{H} = -2J_1(\hat{S}_1 \cdot \hat{S}_2 + \hat{S}_3\hat{S}_4) - 2J_2\hat{S}_2\hat{S}_3 + D(\hat{S}_{2z}^2 + \hat{S}_{3z}^2) - g\mu_B(\hat{S}_1 + \hat{S}_2 + \hat{S}_3 + \hat{S}_4)H \quad (5)$$

where S_1 and S_4 are the Mn^{II} spins and S_2 and S_3 are Mn^{III} spins. Matrix elements are evaluated using a decoupled basis set $|Ms_1Ms_2Ms_3Ms_4\rangle$ and diagonalized by a LAPACK subroutine (DSYEV).[80] Since the spin Hamiltonian has axial symmetry we can adopt the usual Gaussian quadrature for the powder average calculation. The directions of magnetic field and the corresponding integration weight are generated by the ORTHPOL package.[81] The results of the diagonalization procedure are shown as solid lines in Figure 6 (bottom). The fitting parameters are: $g = 1.96$, $D/k_B = -3.90$ K, $J_1/k_B = 9.52$ K, $J_2/k_B = -0.39$ K, with TIP fixed at 600×10^{-6} cm^3 mol^{-1}. The D value obtained is the single-ion D value for Mn^{III} and is consistent with reported values in the literature.[84a] Because J_1 is much greater than J_2, complex **3** can be best visualized as a dimer of dimers. The two feromagnetically coupled dimeric spins, S_A comprised of S_1 and S_2, and S_B comprised of S_3 and S_4, are

---

(79) (a) Boyd, P. D. W.; Martin, R. L. *J. Chem. Soc., Dalton Trans*. **1979**, 92. (b) Gerloch, M.; McMeeking, R. F. *J. Chem. Soc., Dalton Trans*. **1975**, 2443.

(80) Refer for details at http://www.netlib.org/lapack.

(81) Gautsch, W. In *ACM Transactions on Mathematical Software*; 1994, *20*, 21.

(82) (a) Barra, A. L.; Caneschi, A.; Gatteschi, D.; Sessoli, R. *J. Am. Chem. Soc.* **1995**, *117*, 8855. (b) Barra, A. L.; Caneschi, A.; Cornia, A.; Fabrizi de Biani, F.; Gatteschi, D.; Sangregorio, C.; Sessoli, R.; Sorace, L. *J. Am. Chem. Soc.* **1999**, *121*, 5302. (c) Barra, A.-L.; Gatteschi, D.; Sessoli, R. *Phys. Rev. B* **1997**, *56*, 8192. (d) Barra, A.-L.; Caneschi, A.; Gatteschi, D.; Sessoli, R. *J. Magn. Magn. Mater*. **1998**, *177*−*181*, 709.

(83) Belford, B. B.; Belford, R. L.; Burkhalter, J. F. *J. Magn. Reson*. **1973**, *11*, 251.

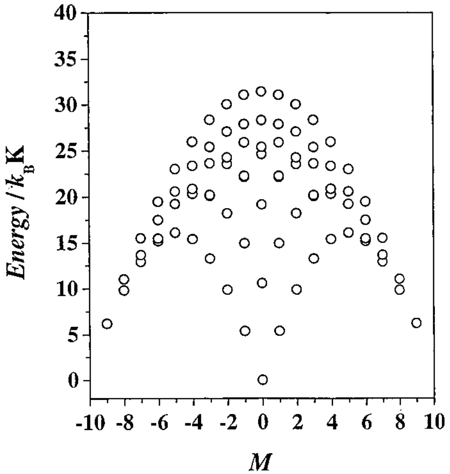

Figure 7. Plot of the energy vs m_z number obtained from fitting the variable field magnetization data for complex **3**. $M_s = 0$ is the lowest in energy and $M_s = \pm 9$ is ca. 6 K above the $M_s = 0$ level.

weakly coupled via the antiferromagnetic interaction J_2. This results in an overall ground state of $S = 0$ because the $S = 9/2$ spins of each dimer cancel. The energy level diagram plotted as energy level vs M_s number of the lowest 100 states of the total 900 states is shown in Figure 7. The M_s number corresponds to the total spin of the dimer of dimer, i.e., $S_A + S_B$. It is seen that the $M_s = 0$ state resulting from antiferromagnetic coupling of the dimers is the lowest energy state and the $M_s = 9$ state is next lowest in energy approximately 6 K above the $M_s = 0$ state. The parameter set obtained from this analysis accommodates the $\chi_M T$ vs temperature data set well. The solid line in Figure 5 corresponds to the fit of the data using the above parameters.

A rationalization for the large saturation of magnetization for complex **3** is as follows. As the energy level diagram shows, the $S = 9$ state is ca. 6 K above the $S = 0$ ground state. The magnetization for complex **3** is influenced largely by Zeeman interactions. In the presence of a magnetic field, components of the states with large spin, i.e., $S = 9$, are stabilized by the Zeeman interactions and can be lower in energy than the zero-field $S = 0$ ground state. In fact, the $S = 9$ state becomes the ground state above a field of 0.5 T. Thus, a high saturation magnetization is observed in the variable field magnetization data. The curvature of the isofield lines in the data for complex **3** reflects the multiple energy levels lying close in energy to the ground state. The isofield lines are essentially flat in the data for complex **2** suggesting a well-isolated ground state. The curvature in the data for complex **3** is likely the result of a population of more than one state in the 2−4 K range.

High-Frequency EPR Spectroscopy. High-frequency EPR (HFEPR) measurements were made to further characterize the ground states of complexes **2** and **3**. In addition to the importance of obtaining direct measurements of both *S* and *D* values, it was of interest to compare the HFEPR spectra for complexes **2** and **1**·2.5H$_2$O. HFEPR is useful in the determination of both the *S* and *D* values of polynuclear complexes with large spin and magnetic anisotropy.[82] Transitions between the M_s levels arising from zero-field splitting in the ground state (see Figure 8) can be observed. These fine structure transitions can be analyzed to obtain both the *S* and *D* values directly; the sign of the zero-field splitting parameter *D* can also be determined. The *S* value can be qualitatively determined by counting the number of the resonances if the fine structure is well resolved and there is enough thermal energy to populate all levels. For a complex with a given *S* value for instance, a total of 2*S* resonances will be observed. The *D* value on the other hand is obtained from the spacing between the resonances and the sign of *D* is obtained from the temperature dependence of the intensities of the fine structure peaks. Thus, a complex with a negative *D* value will give an EPR spectrum with the number of parallel transitions increasing toward high fields when the temperature is increased. The trend is reversed for a complex with a positive *D* value.

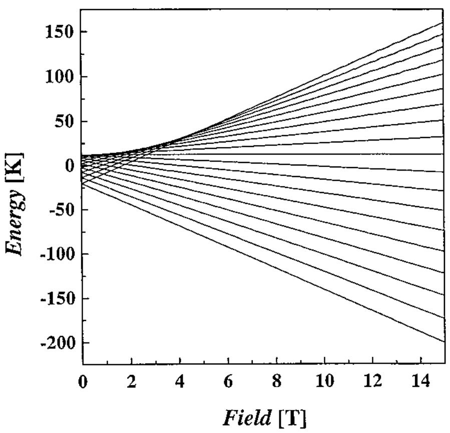

Figure 8. Plot of the energy vs the external field (*H*) for the 19 zero-field split components of the $S = 9$ ground-state assuming $D/k_B = -0.5$ K and $g = 1.99$. The energy level splitting is for a molecule with its principle magnetic axis aligned along the direction of applied magnetic field.

The spin Hamiltonian that describes a molecule with a spin *S* influenced by Zeeman interaction and axial zero-field splitting is given in eq 6:

$$\hat{H} = g\mu_B\hat{S}\cdot H + D[\hat{S}_Z^2 - (1/3)S(S+1)] \qquad (6)$$

where *g* is the Lande factor and μ_B is the Bohr magneton. In this equation, the first term is the Zeeman term and the second term gauges the axial zero-field splitting in the ground state. The resonance lines in a HFEPR spectrum for large spin molecules with uniaxial anisotropy depend on the orientation of the crystallites in the presence of the high magnetic field. The position of these resonances are given by eq 7.

$$H_r = h\nu/g\mu_B - (2M_s + 1)D' \qquad (7)$$

where $h\nu$ is the microwave energy and $D' = [3(\cos^2\theta) - 1]\cdot D/2g\mu_B$ with *g* and μ_B as the usual physical constants and θ being the angle between the easy axis of the molecule in the crystal and the magnetic field. Since single-molecule magnets have such a large magnetic anisotropy, the crystallites usually orient in the presence of strong magnetic fields such that the anisotropy axes of the molecules in the crystal align parallel to the magnetic field. The angle θ is zero if all the anisotropy axes are parallel to the field, however, depending on the orientation of the molecules relative to one another within the crystal, there can be an angle between the molecular anisotropy axis and the field. The angle, if large enough, can alter the

---

(84) (a) Barra, A.-L.; Gatteschi, D.; Sessoli, R.; Abbati, G. L.; Cornia, A.; Fabretti, A. C.; Uytterhoeven, M. G. *Angew. Chem., Int. Ed. Engl.* **1997**, *36*, 2329. (b) Goldberg, D. P.; Telser, J.; Krzystek, J.; Montalban, A. G.; Brunel, L.-C.; Barrett, A. G. M.; Hoffman, B. M. *J. Am Chem. Soc.* **1997**, *119*, 8722. (c) Krzystek, J.; Telser, J.; Pardi, L. A.; Goldberg, D. P.; Hoffman, B. M.; Brunel, L.-C. *Inorg. Chem.* **1999**, *38*, 6121.

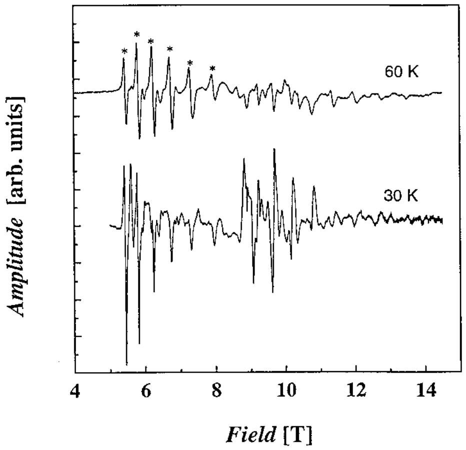

Figure 9. High-frequency EPR spectra for a oriented microcrystalline sample of complex **2** collected at 291.26 GHz and temperatures of 30 and 60 K. The asterisks denote the fine structure resonances due to the transitions between Ms levels of the ground state.

positions of the parallel resonance in the HFEPR spectrum and influence the magnitude of *D*.

HFEPR measurements using the frequencies of 191.30, 291.26, and 388.35 GHz were made for a loosely packed microcrystalline sample of complex **2** to allow torquing. Shown in Figure 9 are quasi single-crystal spectra at 291.26 GHz and either 30 or 60 K. In the 30 K spectrum, two sets of resonances are observed: one set occurring in the 5−8 T region and the other occurring in the 9−12 T region. Most of the resonances in the 9−12 T region are due to the higher frequency harmonics (i.e., 4 times the 95.65 GHz). Independent measurements at 388.35 GHz confirmed that the resonances in the 9−12 T region of the 291.26 GHz spectrum are from the higher harmonics. In the 30 K spectrum, admixture of absorption and derivative signals due to the one-path transmission method complicates the appearance of the spectrum and some of the resonances are not clearly defined. However, it is still evident that there are regularly spaced resonances. These resonances become more evident and well-defined at 60 K. At 60 K, six well-defined resonances are observed in the 5−8 T region as denoted by a asterisks. There is appreciable thermal energy at 60 K to populate higher energy M_s levels, thus more fine structure features are seen at this temperature. Comparison of the spectra at the two temperatures, shows that the resonances observed in the high field region in the 60 K spectrum have larger relative intensities compared to those in the 30 K spectrum. Thus, it can be concluded that $D < 0$ for complex **2**.

HFEPR measurements were also made for a loosely packed microcrystalline sample of complex **3** to see if fine structure resonances were observable for this complex. Shown in Figure 10 is a plot of the HFEPR spectra for complex **3** at the two different frequencies 190.01 and 285.02 GHz at 60 K. The peaks in the 2−6 T region of the 190.01 GHz spectrum are attributed to fine structure transitions. These fine structure transitions are likely from the zero-field split components of the $S = 9$ state which becomes stabilized at high magnetic fields. However, the poor resolution limited a detailed study into the temperature dependence. One possible reason for the poor resolution is incomplete torquing of the sample to give well-resolved parallel signals. Even for magnetically anisotropic complexes such as complex **3**, the manner in which the sample is packed for measurement as well as the size of the crystallites used can impact the orientation of the crystallites in a magnetic field. Because parallel EPR spectra are observed in the field region shown, incomplete orientation of the sample can dramatically influence the line shape and hence resolution of the transitions. Another possibility for the poor resolution is that the spectrum contains a rather large $g = 2$ signal. Detailed experiments are necessary to better understand the origins of the line shape and resolutions in the EPR spectrum of complex **3**.

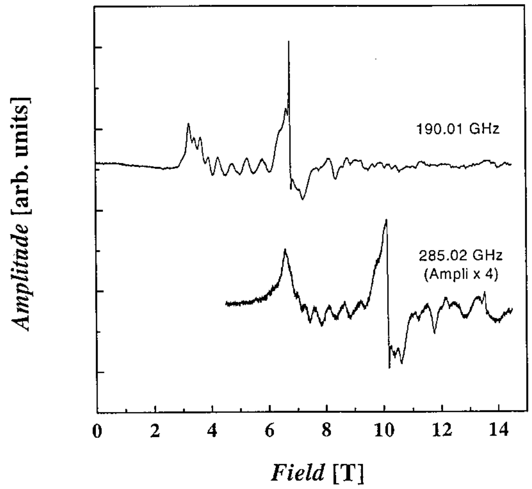

Figure 10. High-frequency EPR spectra for a microcrystalline sample of complex **3** collected at 190.01 and 285.02 GHz and temperature of 60 K.

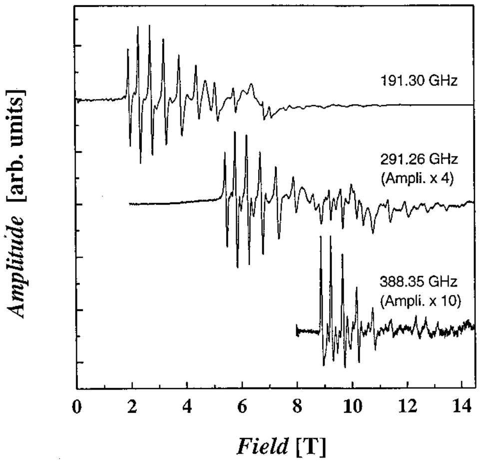

Figure 11. High-frequency EPR spectra for a microcrystalline sample of complex **2** collected at 191.30, 291.26, and 388.35 GHz and temperature of 60 K.

The well-resolved fine structure in the spectra for complex **2** are more amenable for more detailed analysis. Shown in Figure 11 are the results of measurements made at three different frequencies at 60 K. Regularly spaced transitions attributed to fine structure observed at 191.30 GHz are also seen at 291.26 and 388.35 GHz. Table 4 summarizes the observed resonance positions for the HFEPR spectra for complex **2** at the three frequencies. These resonances correspond to transitions from the M_s to the $(M_s + 1)$ levels of the ground state. Thus, assuming complex **2** has a ground-state spin of $S = 9$ with zero-field splitting, the 1.938 T resonance in the 191.3 GHz spectrum corresponds to the $M_s = -9 \rightarrow M_s = -8$ transition, the 2.308 T resonance corresponds to a $M_s = -8 \rightarrow M_s = -7$ transition, and so on. In the 191.30 GHz spectrum at 60 K, all the transitions up to the $M_s = 0 \rightarrow M_s = +1$ are observed. The other 8 fine structure transitions from $M_s = +1 \rightarrow M_s = +2$ up to $M_s = +8 \rightarrow M_s = +9$ are not observed in part because at 60 K there is little Boltzmann population in these higher energy

Table 4. Resonant Field Transitions for $[Mn_4(hmp)_6Br_2(H_2O)_2]Br_2\cdot 4H_2O$

transition	Resonance Fields					
	191.30 GHz		291.26 GHz		388.35 GHz	
$M_s \rightarrow M_s + 1$	exp	calc	exp	calc	exp	calc
$-9 \rightarrow -8$	1.938	1.8796	5.437	5.4687	8.873	8.9544
$-8 \rightarrow -7$	2.308	2.2073	5.797	5.7963	9.232	9.2821
$-7 \rightarrow -6$	2.73	2.6321	6.222	6.2212	9.656	9.7069
$-6 \rightarrow -5$	3.232	3.1413	6.708	6.7303	10.161	10.2161
$-5 \rightarrow -4$	3.787	3.7217	7.275	7.3107	10.73	10.7965
$-4 \rightarrow -3$	4.405	4.3604	7.913	7.9495		
$-3 \rightarrow -2$	5.069	5.0446	8.616	8.6336		
$-2 \rightarrow -1$	5.75	5.7611	9.205	9.3502		
$-1 \rightarrow 0$	6.403	6.4971				
$0 \rightarrow 1$	7.044	7.2396				

levels. It is also possible that the higher energy resonances are obscured by the presence of extra signals. A broad signal is observed at ca. 4.7 and 6.1 T in the 191.30 GHz spectrum (Figure 11). The broad signal at ca. 6.1 T is a shoulder of a resonance at 6.403 T which is assigned as the $M_s = -1 \rightarrow M_s = 0$ transition. The broad signals at ca. 4.7 and 6.1 T also appear in the higher harmonics and are real; they are more apparent in the 291.26 GHz spectrum than the 388.35 GHz spectrum. These signals may arise from defect sites in the crystal of complex **2**. The presence of these signals can obscure the fine structure transitions if they directly overlap the transitions at high fields. The reduced number of resonances seen at 388.35 GHz compared to 191.30 GHz is due to less microwave power available resulting in a poor signal-to-noise ratio.

Upon close inspection of the resonance lines at each frequency in Figure 11, it was found that they are not equally spaced. For example, in the 191.30 GHz spectrum the spacing between the resonances increases toward the high field region of the fine structure pattern. This is further evident when the resonance field at which the transitions occur is plotted as a function of M_s. Shown in Figure 12 is a plot of resonance field vs M_s for the data measured at the three frequencies. This plot is made assuming that the first peak in the fine structure is due to a transition from $M_s = -9 \rightarrow M_s = -8$. It is clear from this plot that the resonance field positions do *not* exhibit a linear dependence on M_s, as expected from eq 7. As a result, the longitudinal quartic zero-field splitting term, $(35B_4{}^o\hat{S}_z^4)$, was added to eq 6 to give eq 8:

$$\hat{H} = g\mu_B\hat{S}\cdot H + D[\hat{S}_Z^2 - (1/3)S(S+1)] + 35B^\circ{}_4\hat{S}_Z^4 \tag{8}$$

The resonance field data for all three frequencies were analyzed using eq 8 by employing the eigenfield approach with the downhill simplex method.[83] The solid lines in Figure 12 correspond to the fit of the data. Because the easy axes of neighboring molecules of complex **2** are canted at 9.0 ± 0.5°, the angle between the easy axis of each molecule and the applied field is 4.5°. This angle was taken into account in the analysis. The fit was optimal when all the parameters, g, D, and $B_4{}^o$ were varied, which resulted in $g = 2.03$, $D/k_B = -0.497$ K and $B_4{}^o/k_B = 1.76 \times 10^{-5}$ K. However, these results are not reasonable, for the final g value is greater than 2.00. It is typical to have $g \leq 2$ for manganese complexes.[84] A somewhat poorer fit was obtained by fixing the g value at 1.99 which resulted in D/k_B and $B_4{}^o/k_B$ values of -0.527 K and 2.18×10^{-5} K, respectively. At this point, it was decided that the HFEPR spectra needed to be simulated.

Simulation of HFEPR Spectra. The spectra shown in Figure 11 are parallel spectra arising from torquing of the sample in the magnetic field. Simulations of the HFEPR spectra show that, in addition to the D and $B_4{}^o$ parameters, it was necessary to include rhombic zero-field splitting, $E(\hat{S}_x^2 - \hat{S}_y^2)$, to fit the observed resonance fields for the fine structure. Shown in Figure 13 is the plot of the experimental spectrum (top) together with two simulations for the 191.30 GHz spectrum at 60 K. The canting angle of 4.5° was taken into account in the simulation. The following parameters were initially used to simulate the spectra for a complex with $S = 9$ ground state: $D/k_B = -0.498$ K, $g = 1.999$, and $B_4{}^o/k_B = 1.72 \times 10^{-5}$ K. These parameters are close to those obtained above by fitting the resonance positions to eq 8. The bottom trace in Figure 13 is the simulated spectrum using the parameters: $D/k_B = -0.498$ K, $g = 1.999$, and $B_4{}^o/k_B = 1.72 \times 10^{-5}$ K for an $S = 9$ ground state. It was noticed that the positions of the high field resonances of this simulated spectrum do not correspond well with that of the experimental spectrum. The $M_s = -1$ to $M_s = 0$, and $M_s = 0$ to $M_s = +1$ transitions are seen to be at slightly higher fields in the simulated spectrum compared to the experimental. It was also found that the small resonances at ca. 1.0 T observed in the experimental spectrum do not appear in the simulation. After considerable efforts varying g, D, and $B_4{}^o$, it was concluded

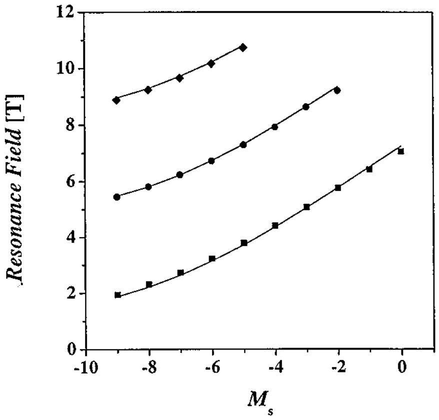

Figure 12. Plots of resonance field vs M_s number for the HFEPR transitions between the M_s and $M_s + 1$ zero-field components of the $S = 9$ ground state for complex **2**. HFEPR data were measured at 191.30 (lowest line), 291.26 (middle line), and 388.35 (highest line) GHz at 60 K. The solid lines represent a fit of the data as described in the text.

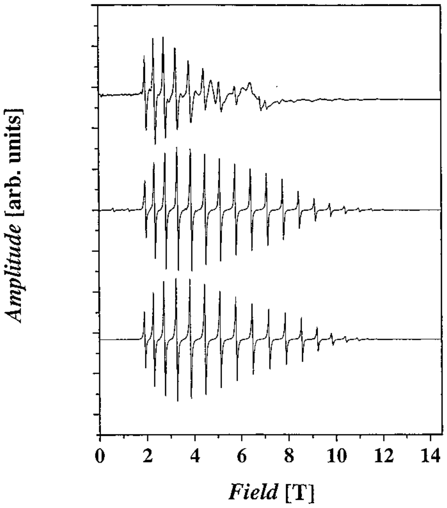

Figure 13. HFEPR spectrum at 191.30 GHz at 60 K (top) and simulation of the spectrum with E term (middle) and without E term (bottom). Simulation results are described fully in the text.

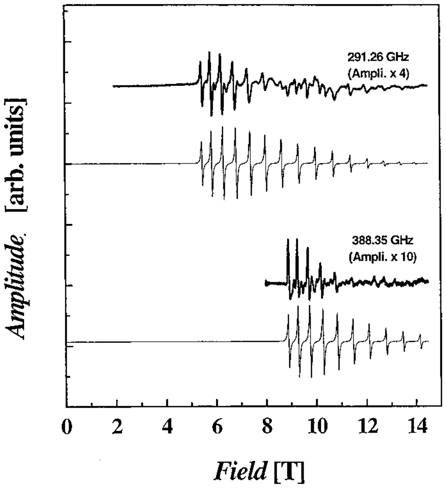

Figure 14. Simulation of the HFEPR spectra at 291.26, and 388.35 GHz frequencies at 60 K. See text for details.

that a rhombic zero-field interaction term was needed. The spectrum was simulated with eq 9:

$$\hat{H} = g\mu_B\hat{S}\cdot H + D[\hat{S}_Z^2 - (1/3)S(S+1)] + E(\hat{S}_x^2 - \hat{S}_y^2) + 35B_4{}^o\hat{S}_z^4 \quad (9)$$

Several different values of g, D, E, and $B_4{}^o$ were tried and the best simulation obtained with eq 7 is shown in Figure 13 (middle trace). The parameters for this simulation are $g = 1.999$, $D/k_B = -0.498$ K, $E/k_B = 0.124$ K, and $B_4{}^o/k_B = 1.49 \times 10^{-5}$ K. The resonance positions for this simulated spectrum are in better agreement with the experimental spectrum. The $M_s = -1$ to $M_s = 0$, and $M_s = 0$ to $M_s = +1$ transitions are better matched between the experimental and simulated spectra. Moreover, the simulated spectrum incorporating the E parameter shows the small resonances at ca. 1.0 T that are seen in the experimental spectrum. Figure 14 shows the simulations of the 291.26 and 388.35 GHz spectra for complex **2**. The simulations were made using the same parameters as those for the 191.30 GHz spectrum. As can be seen, one set of parameters gives good simulations for all the spectra obtained for complex **2**.

Although it was found that the inclusion of E improved the simulation of the HFEPR spectra, it is important to note the magnitude of the E value obtained from the simulation is large. In fact, it is close to the upper limit of $1/3D$ expected for E. Although an E/k_B value of 0.373 K has been determined for a mononuclear Mn^{III} complex from HFEPR measurements,[84a] such a high E value has not been reported for polynuclear Mn complexes. In fact, the E value for the complex, $[Mn_{12}O_{12}(O_2CMe)_{16}(H_2O)_4]\cdot 4H_2O\cdot 2HO_2CMe$ is nearly zero. Although the simulation of the HFEPR spectra improved with inclusion of E, it should be emphasized that the E value obtained from the simulation is not precise. Inelastic neutron scattering measurements are needed to confirm the precise value of E for complex **2**. The parameter E is very important for SMM's since the magnitude of E can have a profound effect on the rate of magnetization tunneling. The rhombic zero-field interaction, $E(\hat{S}_x^2 - \hat{S}_y^2)$, can mix together M_s states that differ in 2 in M_s values. Thus, this interaction mixes the $M_s = -9$ state with the $M_s = -7$ state, or in general a M_s state and a ($M_s \pm 2$) state. Together with other transverse interaction terms such as transverse (perpendicular) magnetic field, rhombic zero-field interactions determine the rate of magnetization tunneling between the $2S + 1$ levels in the ground state (Figure 1).

The simulation was able to reproduce the experimental resonance positions accurately, however, there appears some disagreement in the amplitudes of the individual resonance lines between experiment and simulations. The amplitude of the experimental resonance lines decreases much more rapidly toward high fields than seen in the simulation. This discrepancy may be due to resonance line width. The line width of the $M_s = -9$ to $M_s = -8$ transition is measured to be ca. 600 G broad. The $M_s = -3$ to $M_s = -2$ transition is ca. 900 G broad. The line width of the transitions observed above 10.0 T, assuming that they are a part of this series, is measured to be 2000 G and up to 3000 G broad. The simulation program does not account for the change in line width at high fields, but assumes a constant line width for the resonances. This is a reason for the reduced amplitude at high fields in the experimental spectrum. The origin of the broadening of the line width is not clear, but perhaps could be due to a relaxation dependence on field or strain effects. Additional experiments are required which are presently ongoing.

AC Magnetic Susceptibility. Variable-field magnetization data and HFEPR spectra showed that complex **2** has a $S = 9$ ground state. Since the $S = 9$ ground state has considerable magnetic anisotropy with $D/k_B = -0.498$ K, a potential energy barrier is present for the reversal of the direction of magnetization in complex **2**. As illustrated in Figure 1, the presence of D splits the $S = 9$ ground state into $M_s = \pm 9, \pm 8, ..., \pm 1, 0$ levels. When $D < 0$, in zero applied field the $M_s = +9$ and $M_s = -9$ levels are the lowest in energy and $M_s = 0$ the highest. Complex **2** should exhibit slow magnetization relaxation in response to a change in direction of the external magnetic field.

AC susceptibility measures the magnetization under an oscillating magnetic field, so it is possible to determine the rate at which a single-molecule magnet reverses its direction of magnetization. A collapse in the in-phase ($\chi_M{}'$) component and an appearance of a peak in the out-of-phase ($\chi_M{}''$) component of the AC magnetic susceptibility are observed when the frequency of the oscillating magnetic field equals the rate at which a single-molecule reverses its direction of magnetization. The initial observations that complex **2** functions as a single-molecule magnet were made with AC susceptibility measurements in the 1.8−6.4 K range employing an MPMS2 magnetometer. These revealed the onset of an out-of-phase AC signal at 1.8 K. These initial observations were followed by AC magnetic susceptibility measurements made on a polycrystalline sample of complex **2** in the 0.05−4.0 K range. Figure 15 gives the results of these AC susceptibility measurements at three different frequencies. At 992 Hz, the in-phase component is about 45 cm^3 mol^{-1} K at 3.5 K and it steadily decreases to about 30 cm^3 mol^{-1} K at around 2 K. This decrease in the 2.0−3.5 K range is attributed to intermolecular antiferromagnetic interactions the effects of which can be observed at low temperatures. This supports what is observed from the X-ray structure for complex **2** which reveals the presence of hydrogen bonding contacts present within the crystal and also small separation between molecules of complex **2**. Such a large drop in the in-phase component was not observed in the analogous complex **1**;[69b] the in-phase component of the AC magnetic susceptibility remained essentially flat at high temperature prior to the onset of spin freezing. Below 2 K, an abrupt drop in the in-phase component for complex **2** is observed from 30 cm^3 mol^{-1} K to near 0 cm^3 mol^{-1} K. The sudden drop in the in-phase component is attributed to a relaxation process as this is accompanied by a peak in the out-of-phase component. At 992 Hz, the peak in the out-of-phase component was observed at

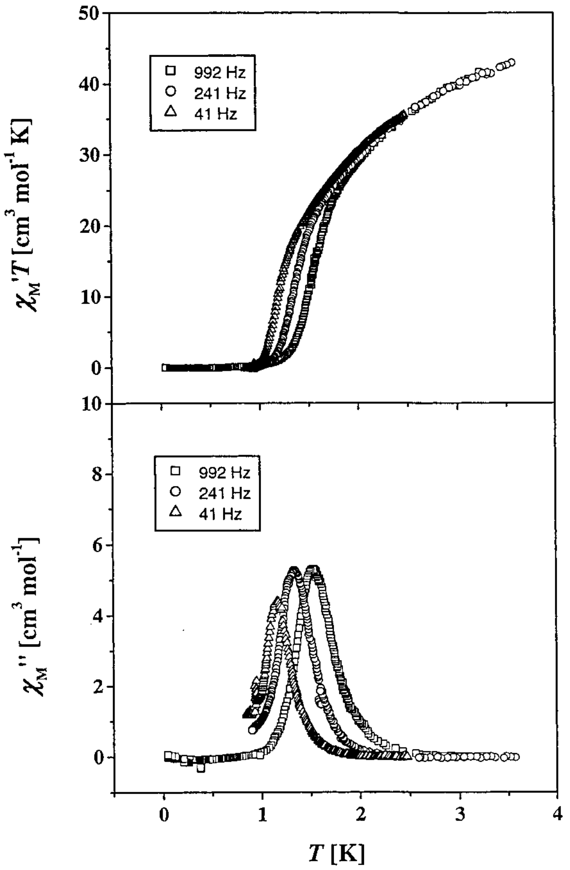

Figure 15. Plots of $\chi_{M'}T$ (top) and $\chi_{M''}$ (bottom) vs temperature for a polycrystalline sample of complex **2** in a 1.0 G AC field oscillating at the indicated frequencies, where $\chi_{M'}$ and $\chi_{M''}$ are the in-phase and out-of-phase components, respectively, of the AC magnetic susceptibility.

Table 5. Out-of-Phase AC Magnetic Susceptibility Results for **2**

$[Mn_4(hmp)_6Br_2(H_2O)_2]Br_2{\cdot}4H_2O$ **(2)**			
AC frequency (Hz)	peak temperature [K][a]	ln(1/τ)[b]	1/*T* [K]
10.5	1.044	−2.3514	0.9579
41	1.170	−3.7136	0.8547
171	1.298	−5.1417	0.7704
241	1.344	−5.4848	0.7441
491	1.399	−6.1964	0.7143
991	1.501	−6.8987	0.6662

[a] This is the temperature where there is a maximum in the out-of-phase AC magnetic susceptibility $\chi_{M''}$. [b] This is the natural logarithm of the inverse of the magnetization relaxation time calculated from the frequency of the AC magnetic field.

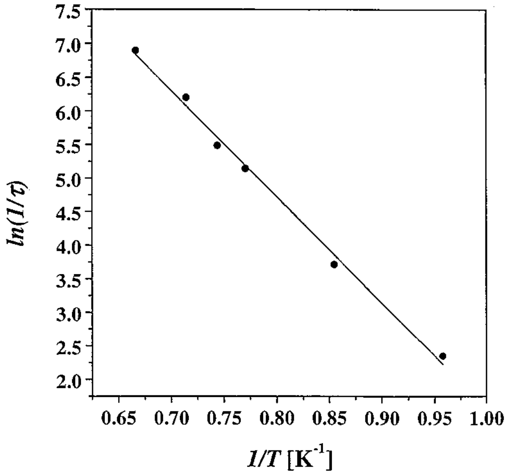

Figure 16. Plot of natural logorithm of the magnetization relaxation rate [ln(1/τ)] vs the inverse of the absolute temperature [K^{-1}]. The solid line represents a least-squares fit of the data to the Arrhenius equation (see text).

1.5 K. This means that at 1.5 K, the rate at which the magnetization reverses its direction is equal to the frequency of the oscillating AC magnetic field. Measurements were made at six different frequencies in the 10.5−992 Hz range to determine the rates of magnetization reversal at different temperatures. The results are summarized in Table 5. It must be noted that complex **2** has a faster rate of spin reversal than complex **1**$\cdot 2.5H_2O$, for the out-of-phase AC response for complex **2** occurs at a lower temperature than was observed for complex **1**$\cdot 2.5H_2O$.[69b] It is possible that the presence of intermolecular interactions is the reason for a faster rate of spin reversal in complex **2** compared to complex **1**$\cdot 2.5H_2O$. Intermolecular exchange interactions may serve as an off-diagonal matrix element responsible for quantum tunneling. It has a similar effect as dipolar interactions, which result from a transverse field exerted from neighboring molecules. Dipolar interactions have been proposed to play a big role in quantum tunneling.[85]

The magnetization relaxation data for complex **2** were analyzed using the Arrhenius law $\tau = \tau_o e^{-\Delta E/k_B T}$. In this equation for the relaxation time τ, Δ*E* is the activation energy, k_B is Boltzmann constant and τ_o is the preexponential factor. Figure 16 gives a plot of ln(1/τ) vs 1/*T*, where the solid line represents the least-squares fit of the data to the Arrhenius equation. From this fit the activation energy Δ*E* was found to be 15.8 K with a preexponential factor of 2.93×10^{-8} s. This value of Δ*E* is to be compared with the thermodynamic barrier of $U/k_B = |D\hat{S}^2|/k_B = 40.3$ K, calculated for complex **2** with the values of $S = 9$ and $D/k_B = -0.498$ K obtained from the simulation of the HFEPR spectra. It is reasonable that *U* is greater than Δ*E*, for the reversal of the direction of magnetization in an SMM may not involve only thermal activation over the potential-energy barrier, but also quantum tunneling of the direction of magnetization.

AC susceptibility measurements were also carried out for complex **3** in the 1.8−6.0 K range employing the MPMS2 magnetometer. Figure 17 shows the results of both the in-phase (top) and out-of-phase (bottom). At 1000 Hz, the in-phase component is about 21 cm^3 mol^{-1} K at 3.5 K and it steadily decreases to about 12 cm^3 mol^{-1} K at around 2 K. This decrease in the 2.0−3.5 K range is attributed to intermolecular antiferromagnetic interactions perhaps propagated by van der Waal interactions between the ligands of neighboring molecules of complex **3** in the crystal. No signs of a drop in the in-phase component and a rise in the out-of-phase component of the AC susceptibility were observed at 1.8 K. The absence of an out-of-phase signal is attributed to the $S = 0$ ground state of complex **3** at zero-field.

It is important to compare the values of *U* and Δ*E* obtained for complex **2** with those obtained for other manganese SMM's. The analogous complex $[Mn_4(pdmH)_6(O_2CCH_3)_2](ClO_4)_2{\cdot}2.5H_2O$ (**1**$\cdot 2.5H_2O$) was determined[69b] with HFEPR data to have $S = 9$ ground state with $D/k_B = -0.45$ K. This gives a thermodynamic barrier of $U/k_B = 36.5$ K for **1**$\cdot 2.5H_2O$ compared to $U/k_B = 40.3$ K for **2**. Similarly, **1**$\cdot 2.5H_2O$ was

---

(85) (a) Prokof'ev, N. V.; Stamp, P. C. E. *Phys. Rev. Lett.* **1998**, *80*, 5794. (b) Cuccoli, A.; Fort, A.; Rettori, A.; Adam, E.; Villain, J. *Eur. Phys. J. B*, **1999**, *12*, 39. (c) Ohm, T.; Sangregorio, C.; Paulsen, C. *Eur. Phys. J. B* **1998**, *6*, 195.

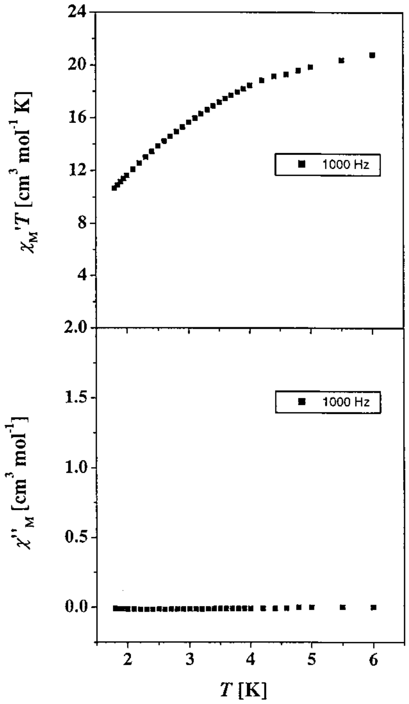

Figure 17. Plot of the in-phase (top) and out-of-phase (bottom) components of the AC magnetic susceptibility for complex **3** in the 1.8−6.0 K range in a 1 G AC field oscillating at 1000 Hz.

reported to have an activation energy for reversal of magnetization of $\Delta E/k_B = 16.7$ K, compared to a value of $\Delta E/k_B = 15.8$ K for complex **2**. The smaller ΔE value for **2** is consistent with the observation of χ_M'' signals at lower temperatures than observed for complex **1**·2.5H_2O, implying that **2** has a faster rate of magnetization reversal. The desolvated form of complex **1** has a $S = 8$ ground state with $D/k_B = -0.35$ K and $U/k_B = 22.4$ K and it has been determined with AC susceptibility data to have $\Delta E/k_B = 17.3$ K. Preliminary magnetization relaxation measurements[70] show that the desolvated complex **1** exhibits a temperature-independent magnetization relaxation rate of 1×10^{-4} s^{-1}. Detailed magnetization decay measurements are being carried out on complex **2**.

Concluding Comments

One of the goals of this research was to synthesize new manganese based single-molecule magnets using nitrogen−oxygen chelate ligands analogous to pyridine-dimethanol (pdmH$^-$). The motivation behind the use of similar ligands stems from the discovery that a new manganese structural type was found with the ligand pdmH$^-$, complex **1**, and that this new complex is a single-molecule magnet. Two new types of manganese complexes are reported in this study. Complex **2** was obtained using monoanionic hydroxymethyl pyridine (hmp$^-$) as the ligand and complex **3** was obtained using a methylated version of hmpH, 6-methyl-hydroxymethyl pyridine. Although hmpH and 6-me-hmpH are both structural analogues of pdmH$^-$, they give complexes with completely different core topologies. The cation in complex **2** is a tetranuclear manganese complex that bears close structural resemblance to the cation in complex **1**. However, complex **3** bears no resemblance to **1** and **2**; it has four Mn ions arranged in a bent chain.

The magnetization characteristics of both complexes **2** and **3** are reported. Complex **2** has an $S = 9$ ground state, whereas complex **3** has an $S = 0$ ground state in small external magnetic fields. HFEPR measurements were made and the data for complex **2** were analyzed which showed that the $S = 9$ and $D/k_B = -0.498$ K values are comparable to those reported for **1**·H_2O. Complex **2** shows frequency-dependent out-of-phase AC susceptibility signals characteristic of single-molecule magnets. Interestingly, the maximum in the out-of-phase magnetic susceptibility signal observed with a 1 kHz oscillating field occurs at a lower temperature for complex **2** than for complex **1** and its hydrate.

Even though complex **2** and **1**·H_2O have comparable potential-energy barriers ($U/k_B = 36.5$ K for **1**·H_2O and $U/k_B = 40.3$ K for **2**), complex **2** exhibits a faster magnetization relaxation rate. This may be due to the presence of rhombic zero-field splitting, $E(\hat{S}_x^2 - \hat{S}_y^2)$, for complex **2**. It may also arise from transverse components of dipolar fields within the crystal of complex **2** as well as hyperfine interactions derived from nuclear spins in the molecule.

Acknowledgment. D.N.H. and G.C. thank the National Science Foundation for support of this research.

Supporting Information Available: A table listing all the 110 different spin states for complex **2** used in the least-squares fitting of the magnetic susceptibility data shown in Figure 3; X-ray crystallographic files in CIF format. This material is available free of charge via the Internet at http://pubs.acs.org.

IC0012928